

---

# CarboNeXT and CarboFormer: Dual Semantic Segmentation Architectures for Detecting and Quantifying Carbon Dioxide Emissions Using Optical Gas Imaging

---

Taminul Islam<sup>1</sup>, Toqi Tahamid Sarker<sup>1</sup>, Mohamed G Embaby<sup>2</sup>, Khaled R Ahmed<sup>1</sup>, Amer AbuGhazaleh<sup>2</sup>

<sup>1</sup>School of Computing, <sup>2</sup>School of Agricultural Sciences  
Southern Illinois University, Carbondale, USA

{taminul.islam, toqitahamid.sarker, mohamed.embaby, khaled.ahmed, aabugha}@siu.edu

## Abstract

Carbon dioxide (CO<sub>2</sub>) emissions are critical indicators of both environmental impact and various industrial processes, including livestock management. We introduce CarboNeXT, a semantic segmentation framework for Optical Gas Imaging (OGI), designed to detect and quantify CO<sub>2</sub> emissions across diverse applications. Our approach integrates a multi-scale context aggregation network with UPerHead and auxiliary FCN components to effectively model both local details and global relationships in gas plume imagery. We contribute two novel datasets: (1) the Controlled Carbon Dioxide Release (CCR) dataset, which simulates gas leaks with systematically varied flow rates (10-100 SCCM), and (2) the Real Time Ankom (RTA) dataset, focusing on emissions from dairy cow rumen fluid in vitro experiments. Extensive evaluations demonstrate that CarboNeXT outperforms state-of-the-art methods, achieving 88.46% mIoU on CCR and 92.95% mIoU on RTA, with particular effectiveness in challenging low-flow scenarios. The model operates at 60.95 FPS, enabling real-time monitoring applications. Additionally, we propose CarboFormer, a lightweight variant with only 5.07M parameters that achieves 84.68 FPS, with competitive performance of 84.88% mIoU on CCR and 92.98% on RTA, making it suitable for resource-constrained platforms such as programmable drones. Our work advances both environmental sensing and precision livestock management by providing robust tools for CO<sub>2</sub> emission analysis, with a specific focus on livestock applications.

## 1 Introduction

Climate change mitigation and greenhouse gas management remain some of the most pressing challenges facing global environmental sustainability. Among various greenhouse gases, carbon dioxide (CO<sub>2</sub>) significantly contributes to global warming, necessitating precise and efficient monitoring and quantification techniques to support emission reduction strategies [1]. National Aeronautics and Space Administration (NASA) reports that CO<sub>2</sub> accounts for approximately 80% of greenhouse gas emissions from human activities. Since the pre-industrial era (around 1750), atmospheric CO<sub>2</sub> concentrations have increased by about 50% [2]. Traditional methods for quantifying CO<sub>2</sub> emissions typically rely on expensive, cumbersome, and laboratory-centric instruments, such as Fourier-transform infrared (FTIR) spectrometers [3], which severely limit their practical applicability in diverse real-world conditions and field environments.

Recent advances in computational methodologies have addressed some traditional approach limitations, including machine learning techniques for optimizing CO<sub>2</sub> capture materials [4], deep

learning models for predicting vehicle emission [5], and methods for quantifying geological carbon sequestration in basalt reservoirs with 60% effectiveness [6]. However, these methods remain limited by specific datasets and high computational requirements. On the other hand, computer vision has expanded real-time gas detection possibilities through subsea leak detection using Faster R-CNN and YOLOv4 [7], infrared imaging with segmentation networks for butene detection [8], and zero-shot detection of methane using synthetic datasets [9], though concerns remain about real-world applicability for CO<sub>2</sub> detection specifically.

To effectively identify and quantify CO<sub>2</sub> emissions at lower flow rates, such as those typically emitted by livestock, it is essential to utilize sophisticated image segmentation methodologies. Semantic segmentation, a robust technique [10] in computer vision that involves assigning specific class labels to every pixel in an image, has successfully addressed complex challenges across diverse domains, including medical imagery [11], agriculture [12, 13, 14], and remote sensing [15, 16] applications. Initially, Fully Convolutional Networks (FCN) significantly advanced the field of semantic segmentation [17] by facilitating seamless, end-to-end model training. More recently, however, transformer-based architectures, especially Vision Transformers (ViT) [18], have gained prominence, exhibiting superior performance compared to conventional Convolutional Neural Networks (CNNs) in image classification, object detection, and segmentation tasks.

Motivated by the need for precise CO<sub>2</sub> quantification for agricultural management and animal health monitoring, we investigate OGI techniques combined with semantic segmentation. We curate two datasets: (1) **Controlled Carbon Dioxide Release (CCR)** dataset, featuring systematic CO<sub>2</sub> emissions captured via FLIR G343 OGI camera [19] under varied flow rates, and (2) the **Real Time ANKOM (RTA)** dataset, containing real-time CO<sub>2</sub> emissions from dairy cow rumen fluid experiments using the ANKOM gas production module [20].

To address the challenges of CO<sub>2</sub> plume detection, in this study, we propose two architectures: CarboNeXT and CarboFormer. **CarboNeXT** employs a multi-scale transformer-based encoder-decoder structure with UPerHead and auxiliary FCN head for high-precision segmentation. **CarboFormer**, its lightweight counterpart, maintains competitive accuracy while optimizing for resource-constrained platforms through efficient attention mechanisms and model compression. Both models explicitly detect CO<sub>2</sub> for accurate plume delineation across varying flow rates, with CarboNeXT prioritizing detection accuracy and CarboFormer balancing performance with computational efficiency.

The main contributions of our study include:

1. We introduce CarboNeXT, a robust semantic segmentation model designed explicitly for segmenting and quantifying CO<sub>2</sub> emissions from OGI imagery, along with CarboFormer, a lightweight variant optimized for resource-constrained platforms such as programmable drones.
2. We create two distinctive and comprehensive datasets (CCR and RTA) to facilitate accurate CO<sub>2</sub> plume segmentation and quantification, with particular focus on the previously unexplored domain of livestock emissions.

## 2 Related Work

**Traditional CO<sub>2</sub> detection methods** [21, 22, 23, 24, 25, 26] have established a strong foundation in environmental monitoring through well-validated physical and chemical principles. Nondispersive infrared (NDIR) sensing remains the dominant approach, exploiting CO<sub>2</sub>'s characteristic infrared absorption properties. Recent advances in NDIR technology include CMOS-compatible MEMS pyroelectric detectors [27] and chamberless designs robust against environmental fluctuations [28]. Comprehensive evaluations of low-cost NDIR sensors by [29] have demonstrated their potential for widespread deployment, while specialized applications such as human respiration monitoring have been achieved through portable solid-state designs [30]. Advanced techniques like tunable diode laser absorption spectroscopy (TDLAS) and off-axis integrated cavity output spectroscopy (OA-ICOS) have further expanded the capabilities of physical detection methods [31].

**Deep learning approaches** [32, 7, 13, 33, 34, 4] have revolutionized environmental monitoring by addressing limitations of traditional methods. Vision Transformers [18] introduced self-attention mechanisms that excel at capturing both local features and global context in image data. These architectures have been particularly effective in gas plume detection, where the ability to process complex spatial relationships is crucial. Recent work in semantic segmentation has demonstrated significant

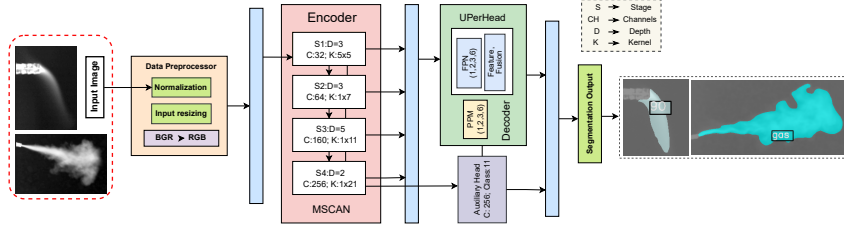


Figure 1: **Architecture of CarboNeXT.** The encoder employs MSCAN with four stages ( $S_1$ - $S_4$ ) with increasing embedding dimensions (C), varying depths (D), and kernel sizes (K). The decoder uses UPerHead which incorporates PPM and FPN components to fuse multi-scale features. An auxiliary head connected to  $S_3$  provides additional supervision during training, with the final output producing the segmentation map and flow-rate classification.

improvements through multi-scale feature aggregation [35] and efficient attention mechanisms [36]. The integration of deep learning with IoT frameworks has enabled real-time monitoring capabilities, as demonstrated by [21] in industrial settings and [24] in environmental monitoring applications.

Recent advancements in  $\text{CO}_2$  monitoring span both hybrid sensing systems and environmental applications. **Hybrid sensing systems** [33, 26, 25, 5, 22, 37] combine traditional sensors with AI-enhanced processing, demonstrating success in smart buildings [26, 38] through  $\text{CO}_2$  and light sensor fusion for occupancy estimation and activity pattern recognition. Medical applications have benefited significantly, particularly in transcutaneous monitoring [22] and clinical procedures [23]. In **environmental and industrial domains** [39, 31, 4, 5, 34, 7], significant innovations include geological sequestration monitoring using multivariate regression [39], industrial emission tracking [31], and material optimization through machine learning [4]. Advanced systems like ARTEMON [34] have enabled comprehensive greenhouse gas monitoring, while computer vision approaches have enhanced subsea leak detection [7], demonstrating the versatility of AI-driven  $\text{CO}_2$  monitoring across different applications.

**Despite these advances**, a significant research gap exists in the quantification of  $\text{CO}_2$  emissions using semantic segmentation techniques combined with Optical Gas Imaging (OGI) [40], particularly for agricultural sources. Current methods face limitations in detecting and accurately quantifying the subtle thermal signatures of  $\text{CO}_2$  at minimal flow rates, such as those emitted by livestock. Additionally, **no published research** has utilized semantic segmentation to detect and quantify  $\text{CO}_2$  emissions from dairy cow rumen fluid, which represents a critical area for agricultural management and animal health monitoring. Our research addresses this gap through specialized transformer-based architectures. By leveraging advanced semantic segmentation techniques and novel datasets specifically designed for low-flow scenarios, we enable precise quantification of  $\text{CO}_2$  emissions in agricultural settings, opening new possibilities for animal health monitoring through respiratory pattern analysis.

### 3 CarboNeXT

Our proposed model, CarboNeXT, is based on the encoder-decoder architecture for semantic segmentation as illustrated in Figure 1. The model’s encoder uses a Multi-Scale Context Aggregation Network (MSCAN) [41] to extract multi-scale features from input images, and a decoder combines a Unified Perceptual Parsing Head (UPerHead) [42] with an auxiliary FCN [43] head to generate the final segmentation map.

#### 3.1 Encoder

The encoder employs MSCAN [41] to generate multi-scale feature representations. Input images undergo preprocessing with normalization and resizing to  $512 \times 512$  pixels. This backbone consists of four sequential stages ( $S_1$ - $S_4$ ) with progressive scaling:  $S_1(32, 3, 5 \times 5)$ ,  $S_2(64, 3, 1 \times 7)$ ,  $S_3(160, 5, 1 \times 11)$ , and  $S_4(256, 2, 1 \times 21)$ , where each tuple represents (embedding dimension, depth, attention kernel size). **Multi-Scale Attention** [44] in each stage is formulated as:

$$\text{Attention}(Q, K, V) = \text{SoftMax} \left( \frac{Q \cdot f_k(K)^T}{\sqrt{d}} \right) \cdot f_v(V) \quad (1)$$

where  $f_k$  and  $f_v$  are kernel transformations with stage-specific sizes, and  $d$  denotes feature dimension.

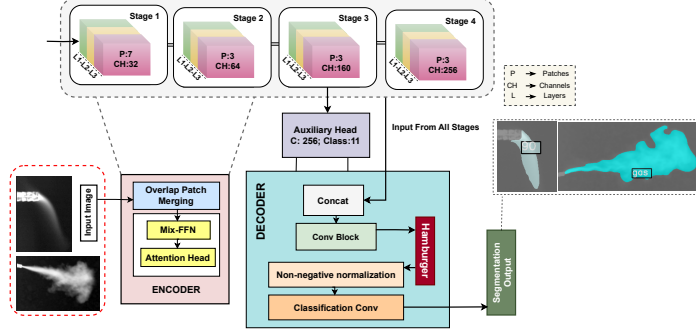


Figure 2: **Architecture of CarboFormer.** The encoder employs a MViT with four stages (S1-S4) with increasing embedding dimensions and varying numbers of attention heads. The decoder uses a LightHAM to process multi-scale features. An auxiliary head connected to S3 provides additional supervision during training. The overlap patch merging and attention mechanisms enable effective feature extraction from input images, with the final output producing the segmentation map and flow-rate classification.

**Feature Hierarchy** generates multi-scale feature maps  $\{F_i\}_{i=1}^4$  with resolutions  $\{\frac{H}{2^{i+1}}, \frac{W}{2^{i+1}}\}_{i=1}^4$  relative to input dimensions  $H \times W$ . The architecture employs MLP ratios  $\{r_i\}_{i=1}^4 = [8, 8, 4, 4]$  and drop path rate  $\rho = 0.1$  for regularization. This hierarchical design enables efficient feature extraction across scales  $\mathcal{S} = \{s_i | s_i = 2^{i+1}, i \in [1, 4]\}$ , capturing both fine-grained details and high-level semantics crucial for gas plume segmentation. The combination of multi-scale attention and progressive feature extraction achieves an optimal balance between computational efficiency and segmentation accuracy, particularly beneficial for real-time gas monitoring applications.

### 3.2 Decoder

The decoder transforms the multi-scale features from the encoder into the final segmentation mask through two primary components: (a) UPerHead [42], and (b) Auxiliary FCN head.

**UPerHead** [42] transforms multi-scale features through Pyramid Pooling Module (PPM) and Feature Pyramid Network (FPN). The PPM captures global context via average pooling with pool sizes  $P = \{1, 2, 3, 6\}$ , where each pooled feature  $f_p, p \in P$  undergoes dimension reduction:  $f'_p = \text{Conv}_{1 \times 1}(f_p, 512)$ , followed by upsampling to original dimensions. The FPN integrates features from encoder stages  $\{S_i\}_{i=1}^4$  through channel unification:  $F_i = \text{Conv}_{1 \times 1}(S_i, 512)$  and progressive upsampling, enabling hierarchical feature fusion crucial for gas plume segmentation.

**Auxiliary FCN Head** operates on stage 3 features, transforming 160 channels to 256 through  $\text{Conv}(F_{S3}, 256)$ , with dropout ratio  $\rho = 0.1$  for regularization.

**Loss Function** combines main and auxiliary supervision:

$$\mathcal{L} = \mathcal{L}_{main} + \lambda \mathcal{L}_{aux} \quad (2)$$

where  $\mathcal{L}_{main}$  and  $\mathcal{L}_{aux}$  are cross-entropy losses for respective predictions, with  $\lambda = 0.4$ . The final segmentation mask  $M$  is computed during inference as  $M = \sigma(\text{UPerHead}(F))$ , where  $\sigma$  is the softmax function and  $F$  represents the fused features. This dual-head architecture with weighted loss optimization enables effective feature learning across multiple scales while maintaining computational efficiency.

## 4 CarboFormer

CarboFormer is a lightweight encoder-decoder architecture designed for efficient CO<sub>2</sub> emission detection in resource-constrained environments (Figure 2). The model combines a Mix Vision Transformer (MViT) [45] backbone with a Light Harmonic Aggregation Module (LightHAM) to achieve competitive accuracy while minimizing computational overhead.

### 4.1 Encoder

The encoder utilizes a **Mix Vision Transformer (Mix ViT)** for hierarchical feature extraction. Mix ViT [45] comprises four sequential stages  $\{S_i\}_{i=1}^4$  with progressive scaling:  $S_1(32, 2, 1, 7 \times 7)$ ,  $S_2(64,$

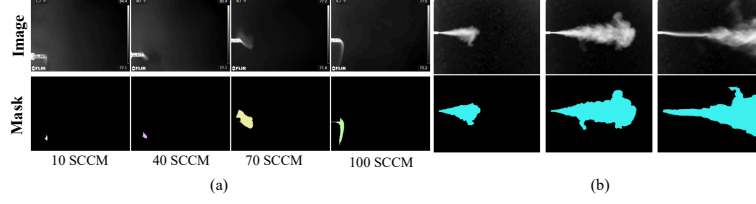


Figure 3: **Dataset visualization.** (a) Controlled carbon dioxide releases in the CCR dataset at different flow rates (10, 40, 70, and 100 SCCM), showing original images (top) and corresponding segmentation masks (bottom). (b) Real-time CO<sub>2</sub> emissions from ANKOM Module in the RTA dataset, demonstrating thermal plume patterns (top) and their ground truth masks (bottom).

2, 2, 3×3),  $S_3(160, 2, 5, 3\times 3)$ , and  $S_4(256, 2, 8, 3\times 3)$ , where each tuple represents (embedding dimension, transformer layers, attention heads, patch size). **Overlap Patch Merging** [46] preserves spatial continuity through:

$$P_i = \mathcal{M}(X, s_i, k_i) \quad (3)$$

where  $\mathcal{M}$  is the merging operation with stride  $s_i$  and kernel size  $k_i$  at stage  $i$ .

**Mix-FFN and Feature Hierarchy** combines MLP layers with depth-wise convolutions, utilizing spatial reduction ratios  $\{r_i\}_{i=1}^4 = [8, 4, 2, 1]$  and MLP ratio 4 across all stages. The architecture generates multi-scale features  $\{F_i\}_{i=1}^4$  with dimensions  $\{d_i\}_{i=1}^4 = [32, 64, 160, 256]$  and drop path rate  $\rho = 0.1$ .

## 4.2 Decoder

**LightHAM** efficiently processes multi-scale features through harmonic aggregation with parameters  $\{\text{MD\_S} = 1, \text{MD\_R} = 16, \text{steps} = 7\}$ . The feature transformation can be expressed as:

$$F_{out} = \text{LightHAM}(\{F_i\}_{i=1}^4) = \sum_{i=1}^4 w_i \cdot T_i(F_i) \quad (4)$$

where  $T_i$  represents stage-specific transformations and  $w_i$  are learnable weights. **Auxiliary FCN Head** provides additional supervision during training, helping the model learn more discriminative features in the early stages while maintaining computational efficiency.

## 5 Dataset

### 5.1 FLIR G343 Optical Gas Imaging Camera

Our experiments utilize the FLIR G343 [19] OGI camera, a specialized cooled mid-wave infrared (MWIR) system operating in the 4.2-4.4  $\mu\text{m}$  spectral range, aligned with CO<sub>2</sub>'s primary absorption band (4.3  $\mu\text{m}$ ). The camera features a 320 × 240 pixel quantum detector with thermal sensitivity of < 15 mK Noise Equivalent Temperature Difference [47].

**Detection Parameters and Range.** The camera's Noise Equivalent Concentration Length (NECL) sensitivity threshold of 30-50 ppm-m for CO<sub>2</sub> establishes the minimum detectable gas concentration over a one-meter path length. The cooled quantum detector enables visualization of CO<sub>2</sub> plumes at distances up to several hundred meters by measuring absorbed infrared radiation, making it suitable for excellent laboratory measurements in our dataset collection.

### 5.2 Controlled Carbon Dioxide Release Dataset

The Controlled Carbon dioxide Release (CCR) dataset was created using a systematic protocol with the FLIR G343 camera under controlled conditions. CO<sub>2</sub> was released from a high-purity calibration gas cylinder (UHP 99.995%, 300L) at a fixed distance of  $\pm 20$  inches, with ambient temperature maintained at  $\pm 86$ -90°F and gas pressure at  $\pm 14.09$  PSIA.

Gas flow was regulated using a Cole-Parmer Digital Pressure Controller (0-15 psi, 1/8" NPT(F)), with rates varying from 10 to 100 SCCM in 10 SCCM increments. Each experiment included a 10-second background video capture for noise isolation, resulting in 20 distinct video sequences. The dataset comprises **19,731 images** (640×480 pixels) captured using multiple FLIR visualization modes (White hot, Black hot, and Lava), with examples shown in Figure 3 (a). Detailed dataset statistics are provided in the Appendix section.

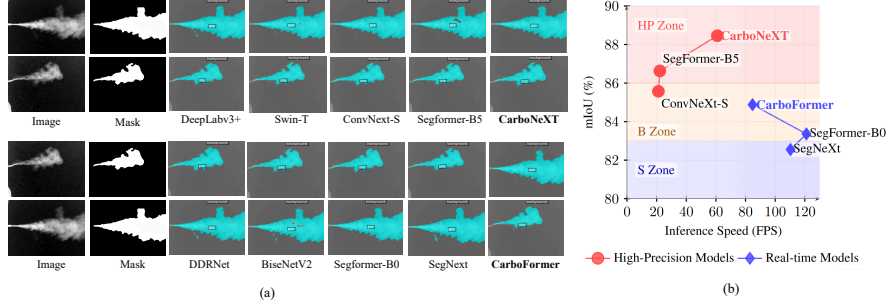


Figure 4: (a) Segmentation results on the RTA dataset comparing different CO<sub>2</sub> detection models. (b) Real-time performance analysis showing the trade-off between inference speed and mIoU (%), with three operational zones: HP (High Performing), B (Balanced), and S (Standard).

Table 1: Comparison of segmentation models on the CCR dataset. Models are divided into heavy-weight (top) and light-weight (bottom) categories. Our models achieve superior performance with CarboNeXT achieving the best overall metrics, while CarboFormer leads the light-weight category with best accuracy and competitive efficiency.  $\uparrow$  indicates higher is better,  $\downarrow$  indicates lower is better.

Model	Aux Head	Neck	mIoU $\uparrow$	mAcc $\uparrow$	mFscore $\uparrow$	FLOPs $\downarrow$	Params $\downarrow$	FPS $\uparrow$
DeepLabv3+ [36]	$\checkmark$	$\times$	81.14	83.77	89.41	270.00G	65.74M	88.64
Swin-T [49]	$\checkmark$	$\checkmark$	83.97	89.07	91.12	260.00G	80.27M	30.61
ConvNeXt-S [50]	$\checkmark$	$\checkmark$	86.57	87.96	92.74	257.00G	80.95M	21.18
SegFormer-B5 [32]	$\times$	$\times$	86.63	90.83	92.67	74.63G	81.98M	22.16
<b>CarboNeXT (Ours)</b>	$\checkmark$	$\times$	<b>88.46</b>	91.04	<b>93.81</b>	214.00G	31.71M	60.95
BiseNetV2 [51]	$\checkmark$	$\times$	74.94	83.18	85.24	12.36G	3.36M	161.39
DDRNet [52]	$\times$	$\times$	73.43	81.11	84.25	4.56G	5.73M	162.10
FastSCNN [53]	$\checkmark$	$\checkmark$	50.15	60.31	65.52	0.94G	1.40M	237.85
SegFormer-B0 [32]	$\times$	$\times$	83.36	90.44	90.76	7.92G	3.72M	121.06
SegNeXt [54]	$\times$	$\times$	82.55	87.91	90.18	6.45G	4.26M	110.32
<b>CarboFormer (Ours)</b>	$\checkmark$	$\times$	84.88	<b>91.13</b>	91.90	11.39G	5.07M	84.68

### 5.3 Real Time Ankom Dataset

The Real Time ANKOM (RTA) dataset captures CO<sub>2</sub> emissions from dairy cow rumen fluid using the ANKOM gas production system [20]. The experimental protocol [48] involved 24-hour anaerobic incubation with controlled pH variations (6.5 to 5.0 in 0.3 increments) to generate diverse CO<sub>2</sub>/CH<sub>4</sub> concentrations. Gas releases were executed in single-shot bursts (0.9 PSI, 250 ms) and captured using the FLIR G343 camera positioned at  $\pm 20$  inches from the source, as shown in Figure 3(b).

The dataset comprises **613 images** (640 $\times$ 480 pixels) with binary labels (gas v/s background), split into training (80%), testing (10%), and validation (10%) sets. While compact, this dataset provides crucial evaluation data for segmentation performance under realistic conditions with varying gas concentrations and dispersion patterns.

### 5.4 Mask Creation

We developed a robust semi-automated pipeline for generating pixel-precise CO<sub>2</sub> plume masks through differential background modeling. For each sequence, we compute a temporal average  $\mu_B$  of  $n$  background frames captured before gas release:

$$\mu_B(x, y) = \frac{1}{n} \sum_{i=1}^n B_i(x, y) \quad (5)$$

where  $B_i(x, y)$  represents the intensity value at pixel coordinates  $(x, y)$  in the  $i$ -th background frame. We isolate potential plumes by subtracting this background model from each foreground frame  $F(x, y)$ , followed by contrast normalization and adaptive histogram equalization. We apply locally adaptive thresholding with sensitivity parameter  $\tau$  calibrated per flow rate category. This calibration is critical, as lower flow rates (10-30 SCCM) require more sensitive thresholds compared to higher flow rates (70-100 SCCM) where thermal signatures are more pronounced.

Table 2: Performance comparison on the RTA dataset. Models are divided into heavy-weight (top) and light-weight (bottom) categories. Our models achieve superior performance with CarboNeXT achieving the best overall metrics, while CarboFormer leads the light-weight category with best accuracy and competitive efficiency.

Model	mIoU(%)	mAcc(%)	mFscore(%)	mPrecision(%)	mRecall(%)	aAcc(%)
DeepLabv3+ [36]	91.68	95.03	95.60	96.20	95.03	96.96
Swin-T [49]	91.15	95.26	95.31	95.36	95.26	96.71
ConvNeXt-S [50]	90.18	93.78	92.68	92.59	94.48	95.22
SegFormer-B5 [32]	92.84	96.37	96.25	96.12	96.37	97.37
<b>CarboNeXT (Ours)</b>	<b>92.95</b>	96.13	<b>97.67</b>	<b>96.23</b>	96.13	97.01
BiseNetV2 [51]	87.95	92.59	93.46	94.42	92.59	95.52
DDRNet [52]	88.28	92.86	93.66	94.52	92.86	95.65
FastSCNN [53]	87.18	91.24	93.00	95.13	91.24	95.31
SegFormer-B0 [32]	92.35	96.00	95.97	95.95	96.00	97.18
SegNeXt [54]	91.16	95.45	95.31	95.17	95.45	96.71
<b>CarboFormer (Ours)</b>	<b>92.98</b>	<b>96.31</b>	<b>96.07</b>	<b>96.84</b>	<b>95.31</b>	<b>97.00</b>

For boundary delineation, we implement the watershed algorithm [55] guided by Sobel-generated gradient magnitude maps. Post-processing includes morphological operations with structuring elements proportional to estimated plume dimensions, followed by region properties filtering based on area, eccentricity, and solidity. The final binary masks undergo a validation check comparing their spatial and temporal consistency with physically plausible gas dispersion models [Figure 3].

## 6 Experiments

### 6.1 Implementation Details

We implement our experiments using PyTorch and MMSegmentation [56] on an NVIDIA A100 GPU (80GB) and Intel Xeon Gold 6338 CPU (2.00GHz). Training utilizes AdamW optimizer ( $\text{lr}=6 \times 10^{-5}$ ,  $\beta_1 = 0.9$ ,  $\beta_2 = 0.999$ , weight decay=0.01) with a two-phase learning rate schedule: LinearLR warm-up ( $10^{-6}$  start factor, 1,500 iterations) followed by polynomial decay (power=1.0). Models are trained for 160K iterations with validation every 8K iterations, using batch sizes of 2/1 for training/inference.

Data augmentation includes random resizing (0.5-2.0) and cropping ( $512 \times 512$  pixels). Performance metrics include mean Intersection over Union (mIoU), mean F-score (mF-score), and Frames Per Second (FPS), with model selection based on validation mIoU and real-time inference requirements.

### 6.2 Results

**Evaluation Results on the CCR Dataset.** We evaluate our proposed models against state-of-the-art segmentation models on the CCR dataset (Table 1), categorizing them into heavy-weight and light-weight architectures. The results demonstrate the effectiveness of our approaches across different computational constraints.

In the heavy-weight category, CarboNeXT significantly outperforms existing methods with 88.46% mIoU, surpassing strong baselines like SegFormer-B5 [32] (86.63%) and ConvNeXt-S [50] (86.57%). Notably, CarboNeXT achieves this superior performance with significantly fewer parameters (31.71M) compared to other heavy-weight models (65-82M), operating at 60.95 FPS.

For light-weight architectures, CarboFormer establishes new state-of-the-art results with 84.88% mIoU while maintaining real-time inference at 84.68 FPS. This performance significantly exceeds other efficient models like SegFormer-B0 [32] (83.36% mIoU) and SegNeXt [54] (82.55% mIoU), while requiring only 5.07M parameters. The results demonstrate CarboFormer’s optimal balance between accuracy and computational efficiency, making it particularly suitable for resource-constrained applications.

These improvements are noteworthy given the challenging nature of CO<sub>2</sub> plume detection across various flow rates. Both models demonstrate robust performance, with CarboNeXT excelling in accuracy and CarboFormer providing an efficient solution for practical carbon dioxide monitoring applications.

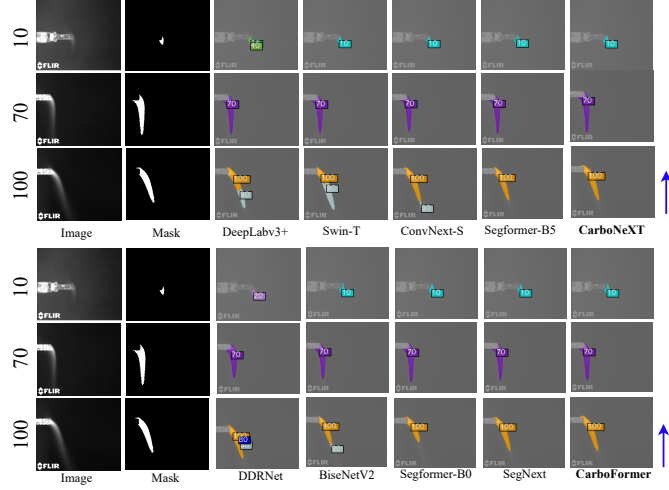


Figure 5: Qualitative comparison of segmentation results on the CCR dataset at different carbon dioxide flow rates (10, 70, and 100 SCCM). For each row, we show the input image, ground truth mask, and predictions from different models. Our proposed CarboNeXT model demonstrates superior boundary preservation and detection accuracy across varying flow conditions.

**Evaluation Results on the RTA Dataset.** To address the limited training data in the RTA dataset (613 images), we employ a transfer learning strategy by first training our models on the larger CCR dataset to establish foundational gas segmentation patterns, then fine-tuning for RTA-specific characteristics.

The comparative analysis on the RTA dataset (Table 2) demonstrates our models’ effectiveness across both categories. In the heavy-weight category, CarboNeXT achieves state-of-the-art performance with 92.95% mIoU and 97.67% mFscore, marginally outperforming SegFormer-B5 [32] (92.84% mIoU). Other heavy-weight models like DeepLabv3+ [36], Swin-T [49], and ConvNeXt-S [50] show strong but lower performance, with mIoU ranging from 90.18% to 91.68%.

In the light-weight category, CarboFormer sets new benchmarks with 92.98% mIoU and 96.07% mFscore, surpassing SegFormer-B0 [32] (92.35% mIoU) and significantly outperforming traditional lightweight architectures like BiSeNetV2 [51], DDRNet [52], and FastSCNN [53] (mIoU < 89%). These results validate our architectural design choices and transfer learning strategy, with both CarboNeXT and CarboFormer excelling in their respective categories while maintaining efficient inference capabilities.

**Qualitative Comparison.** We present qualitative segmentation results on the CCR and RTA datasets in Figure 4 and Figure 5, demonstrating our models’ superior performance across varying experimental conditions. As shown in Figure 3(b), both CarboNeXT and CarboFormer achieve optimal positions in their respective zones (HP and B zones), validating their excellent balance between accuracy and inference speed.

On the CCR dataset, we evaluate performance across different flow rates (10, 70, and 100 SCCM). At low flow rates, baseline models like DeepLabv3+ [36] and DDRNet [52] produce fragmented predictions, while FastSCNN [53] misses subtle plume structures [Figure 5]. Medium flow rates reveal boundary imprecisions in Swin-T [49] and ConvNeXt-S [50], particularly at plume edges. High flow rates expose over-segmentation in BiSeNetV2 [51] and SegNeXt [54], with SegFormer-B5 [32] showing inconsistent boundary delineation. In contrast, CarboNeXT maintains consistent segmentation quality across all flow rates, preserving fine-grained structures and precise boundaries.

The RTA dataset, characterized by complex gas dispersion patterns, further highlights our models’ advantages. It’s clearly visible in Figure 4 (a), traditional architectures (DeepLabv3+ [36], FastSCNN [53]) struggle with intricate boundaries, producing over-smoothed or fragmented predictions. While Swin-T [49] and ConvNeXt-S [50] show improvements, they exhibit boundary imprecisions in regions with rapid intensity gradients. Despite its sophistication, SegFormer-B5 [32] occasionally misses fine structural details. CarboFormer, however, consistently preserves complex plume morphologies while maintaining computational efficiency, demonstrating the effectiveness of our lightweight design.

Table 3: Ablation studies on CarboNeXT and CarboFormer architectural components. MS: Multi-scale feature fusion, 4S: 4-Stage decoder, Ch-512: 512 channel dimension, D-3: 3 transformer layers, S-4: 4-Stage Decoder, Aux-H: auxiliary head. Metrics with  $\uparrow$  indicate higher is better,  $\downarrow$  indicates lower is better.

Configuration	Architecture Design			Performance Metrics					
	MS	4S	Ch-512	mIoU $\uparrow$	mAcc $\uparrow$	mFscore $\uparrow$	FPS $\uparrow$	GFLOPs $\downarrow$	Params $\downarrow$
<i>CarboNeXT Ablations</i>									
Baseline (3-Stage)	✓			87.80	93.60	93.42	61.97	213	30.14
w/ 4-Stage	✓	✓		87.94	91.04	93.50	60.95	214	31.71
w/ Channel-256	✓	✓		87.91	91.88	93.49	62.38	234	30.14
w/o Aux head	✓	✓	✓	82.92	88.90	90.50	60.63	214	31.71
<b>CarboNeXT (Full)</b>	✓	✓	✓	<b>88.46</b>	91.65	<b>93.81</b>	60.95	214	31.71
<i>CarboFormer Ablations</i>									
		D-3	S-4	Aux-H					
w/ Less Layers (D2)		✓		✓	81.22	89.95	90.93	96.00	15.40
w/ 3-Stage Dec		✓			80.13	87.10	88.69	102.65	4.88
<b>CarboFormer (Full)</b>		✓	✓	✓	<b>84.88</b>	91.13	<b>91.90</b>	84.68	11.39

These results validate our architectural choices, showing robust performance in challenging scenarios like boundary precision, detail preservation, and varying flow conditions.

### 6.3 Ablation Study

We conduct comprehensive ablation experiments to analyze key architectural components of both models (Table 3). For **CarboNeXT**, we progressively analyze three core components: multi-scale feature fusion, 4-stage decoder architecture, and channel dimensionality. Starting from a baseline 3-stage model, we observe that the 4-stage decoder enhances performance with minimal computational overhead, while channel dimension adjustments maintain the accuracy-efficiency balance. The auxiliary head proves particularly crucial, as its removal leads to significant performance degradation.

For the lightweight **CarboFormer** variant, we investigate the impact of transformer depth, decoder stages, and auxiliary supervision. Beginning with a baseline 3-stage model, we find that strategically reducing transformer depth while adding layers improves the accuracy-efficiency trade-off. The auxiliary supervision proves beneficial for both architectures, contributing to more stable training and better feature learning.

These studies reveal the complementary nature of our architectural choices: CarboNeXT optimizes for high-performance scenarios through sophisticated feature fusion and deeper architectures, while CarboFormer achieves efficient real-time inference through strategic component selection and model compression. The successful balance between performance and efficiency in both models validates our design decisions for their respective target applications, from high-precision monitoring to resource-constrained deployments.

## 7 Conclusion

In this paper, we presented CarboNeXT and CarboFormer, two complementary semantic segmentation architectures for CO<sub>2</sub> emission detection and quantification using OGI. Our dual-model approach addresses both high-performance requirements and resource-constrained scenarios, with CarboNeXT prioritizing accuracy for critical monitoring applications and CarboFormer enabling real-time detection on programmable drones. The models’ effectiveness in detecting CO<sub>2</sub> emissions, particularly in challenging low-flow conditions, opens new possibilities for environmental monitoring, from industrial leak detection to precision agriculture. While our lightweight CarboFormer demonstrates strong potential for drone-based monitoring, current limitations in its accuracy compared to CarboNeXT and the relatively limited size of our real-world dataset suggest areas for improvement. Future work will focus on expanding the RTA dataset through direct farm measurements with varying pH values, implementing temporal modeling for dynamic gas patterns, and enhancing CarboFormer’s efficiency-accuracy trade-off through advanced knowledge distillation. These advancements will contribute to broader climate change mitigation efforts by enabling more accessible and efficient CO<sub>2</sub> monitoring across agricultural, industrial, and environmental applications.

## References

- [1] Andre Fu, Mahdi S Hosseini, and Konstantinos N Plataniotis. Reconsidering co2 emissions from computer vision. In *Proceedings of the IEEE/CVF Conference on Computer Vision and Pattern Recognition*, pages 2311–2317, 2021.
- [2] NASA. Global Climate Change: Vital Signs of the Planet. <https://climate.nasa.gov/vital-signs/carbon-dioxide/>, 2025. Accessed: June 9, 2025.
- [3] Yulie Liang, Zihan Cao, Shangqi Deng, Hong-Xia Dou, and Liang-Jian Deng. Fourier-enhanced implicit neural fusion network for multispectral and hyperspectral image fusion. *Advances in Neural Information Processing Systems*, 37:63441–63465, 2024.
- [4] Ibrahim B Orhan, Yuankai Zhao, Ravichandar Babarao, Aaron W Thornton, and Tu C Le. Machine learning descriptors for co2 capture materials. *Molecules*, 30(3):650, 2025.
- [5] Gazi Mohammad Imdadul Alam, Sharia Arfin Tanim, Sumit Kanti Sarker, Yutaka Watanobe, Rashedul Islam, MF Mridha, and Kamruddin Nur. Deep learning model based prediction of vehicle co2 emissions with explainable ai integration for sustainable environment. *Scientific Reports*, 15(1):3655, 2025.
- [6] Signe K White, Frank A Spang, H Todd Schaef, Quin RS Miller, Mark D White, Jake A Horner, and B Peter McGrail. Quantification of co2 mineralization at the wallula basalt pilot project. *Environmental Science & Technology*, 54(22):14609–14616, 2020.
- [7] Hongwei Zhu, Weikang Xie, Junjie Li, Jihao Shi, Mingfu Fu, Xiaoyuan Qian, He Zhang, Kaikai Wang, and Guoming Chen. Advanced computer vision-based subsea gas leaks monitoring: a comparison of two approaches. *Sensors*, 23(5):2566, 2023.
- [8] Man Yan, Zhou Li, Zheng Dong, Yiming Liun, Liyun Chen, Xiaosong Wu, and Lijun Wu. Gas leak real-time detection and volume flow quantification based on infrared imaging and advanced algorithms. *IEEE Access*, 13:7284–7292, 2025.
- [9] Wenqi Guo, Yiyang Du, and Shan Du. Langgas: Introducing language in selective zero-shot background subtraction for semi-transparent gas leak detection with a new dataset. *arXiv preprint arXiv:2503.02910*, 2025.
- [10] Tianfei Zhou, Wenguan Wang, Ender Konukoglu, and Luc Van Gool. Rethinking semantic segmentation: A prototype view. In *Proceedings of the IEEE/CVF conference on computer vision and pattern recognition*, pages 2582–2593, 2022.
- [11] Shehan Perera, Pouyan Navard, and Alper Yilmaz. Segformer3d: an efficient transformer for 3d medical image segmentation. In *Proceedings of the IEEE/CVF Conference on Computer Vision and Pattern Recognition*, pages 4981–4988, 2024.
- [12] Antonio Tavera, Edoardo Arnaudo, Carlo Masone, and Barbara Caputo. Augmentation invariance and adaptive sampling in semantic segmentation of agricultural aerial images. In *Proceedings of the IEEE/CVF Conference on Computer Vision and Pattern Recognition*, pages 1656–1665, 2022.
- [13] Toqi Tahamid Sarker, Mohamed G Embaby, Khaled R Ahmed, and Amer AbuGhazaleh. Gasformer: A transformer-based architecture for segmenting methane emissions from livestock in optical gas imaging. In *Proceedings of the IEEE/CVF Conference on Computer Vision and Pattern Recognition*, pages 5489–5497, 2024.
- [14] Peiwen Lin, Peng Sun, Guangliang Cheng, Sirui Xie, Xi Li, and Jianping Shi. Graph-guided architecture search for real-time semantic segmentation. In *Proceedings of the IEEE/CVF conference on computer vision and pattern recognition*, pages 4203–4212, 2020.
- [15] Zhuohong Li, Fangxiao Lu, Jiaqi Zou, Lei Hu, and Hongyan Zhang. Generalized few-shot meets remote sensing: Discovering novel classes in land cover mapping via hybrid semantic segmentation framework. In *Proceedings of the IEEE/CVF Conference on Computer Vision and Pattern Recognition*, pages 2744–2754, 2024.
- [16] Sihan Liu, Yiwei Ma, Xiaoqing Zhang, Haowei Wang, Jiayi Ji, Xiaoshuai Sun, and Rongrong Ji. Rotated multi-scale interaction network for referring remote sensing image segmentation. In *Proceedings of the IEEE/CVF Conference on Computer Vision and Pattern Recognition*, pages 26658–26668, 2024.
- [17] Qiuxiao Chen and Xiaojun Qi. Residual graph convolutional network for bird’s-eye-view semantic segmentation. In *Proceedings of the IEEE/CVF Winter Conference on Applications of Computer Vision*, pages 3324–3331, 2024.

- [18] Alexey Dosovitskiy, Lucas Beyer, Alexander Kolesnikov, Dirk Weissenborn, Xiaohua Zhai, Thomas Unterthiner, Mostafa Dehghani, Matthias Minderer, Georg Heigold, Sylvain Gelly, et al. An image is worth 16x16 words: Transformers for image recognition at scale. *arXiv preprint arXiv:2010.11929*, 2020.
- [19] FLIR Systems, Inc. FLIR G343 Optical Gas Imaging Camera. <https://www.flir.com/products/g343>, 2023. Accessed: June 9, 2025.
- [20] PS Alvarez Hess, P Giraldo, RO Williams, PJ Moate, KA Beauchemin, and RJ Eckard. A novel method for collecting gas produced from the in vitro ankom gas production system. *Journal of Animal Science*, 94:570–570, 2016.
- [21] Mads S-F. Christensen. Leveraging the industrial internet of things (iiot) for real-time co2 monitoring. In *Communications in Computer and Information Science*, pages 35–59. 2025.
- [22] Sara Bernasconi, Alessandra Angelucci, Anastasia De Cesari, Aurora Masotti, Maurizio Pandocchi, Francesca Vacca, Xin Zhao, Chiara Paganelli, and Andrea Aliverti. Recent technologies for transcutaneous oxygen and carbon dioxide monitoring. *Diagnostics*, 14:785, 2024.
- [23] Sergio Cadoni, M.D. Comparison of methods to distend the colon during insertion: Co2, air insufflation, water-aided colonoscopy. <https://clinicaltrials.gov/ct2/show/NCT01954862>, 2013.
- [24] Tiago Araujo, Lgia Silva, and Adriano Moreira. Evaluation of low-cost sensors for weather and carbon dioxide monitoring in iot context. *IoT*, 1:286–308, 2020.
- [25] Francesco Concas, Julien Mineraud, Emil Lagerspetz, Samu Varjonen, Xiaoli Liu, Kai Puolamki, Petteri Nurmi, and Sasu Tarkoma. Low-cost outdoor air quality monitoring and sensor calibration. *ACM Transactions on Sensor Networks*, 17(2):1–44, 2021.
- [26] Q Huang. Occupancy estimation in smart building using hybrid co2/light wireless sensor network, 2017. Unpublished.
- [27] Li Fu, Shixi You, Guangjun Li, and Zengchang Fan. Enhancing methane sensing with ndir technology: Current trends and future prospects. *Reviews in Analytical Chemistry*, 2023.
- [28] Mostafa Vafaei and Amir Amini. Chamberless ndir co2 sensor robust against environmental fluctuations. *ACS Sensors*, 6:1536–1542, 2021.
- [29] Ravish Dubey, Arina Telles, James Nikkel, Chang Cao, Jonathan Gewirtzman, Peter A Raymond, and Xuhui Lee. Low-cost co2 ndir sensors: Performance evaluation and calibration using machine learning techniques. *Sensors*, 24(17):5675, 2024.
- [30] MG Srabanti. Design of a non-dispersive infra-red (ndir) based co2 sensor to detect the human respiratory co2. *Unpublished*, 2019.
- [31] Ning Ding, YanHeng Xi, Wenting Jiang, Hongwei Li, Jun Su, Sixiang Yang, and Tek-Tjing Lie. State-of-the-art carbon metering: continuous emission monitoring systems for industrial applications. *Heliyon*, 2025.
- [32] Enze Xie, Wenhai Wang, Zhiding Yu, Anima Anandkumar, Jose M Alvarez, and Ping Luo. Segformer: Simple and efficient design for semantic segmentation with transformers. *arXiv preprint arXiv:2105.15203*, 2021.
- [33] Yingbo Zhu, Shahriar Abdullah Al-Ahmed, Muhammad Zeeshan Shakir, and Joanna Isabelle Olszewska. Lstm-based iot-enabled co2 steady-state forecasting for indoor air quality monitoring. *Electronics*, 12(1):107, 2022.
- [34] Ali Yavari, Irfan Baig Mirza, Hamid Bagha, Harindu Korala, Hussein Dia, Paul Scifleet, Jason Sargent, Caroline Tjung, and Mahnaz Shafiei. Artemon: Artificial intelligence and internet of things powered greenhouse gas sensing for real-time emissions monitoring. *Sensors*, 23(18):7971, 2023.
- [35] Hengshuang Zhao, Jianping Shi, Xiaojuan Qi, Xiaogang Wang, and Jiaya Jia. Pyramid scene parsing network. In *Proceedings of the IEEE conference on computer vision and pattern recognition*, pages 2881–2890, 2017.
- [36] Liang-Chieh Chen, Yukun Zhu, George Papandreou, Florian Schroff, and Hartwig Adam. Encoder-decoder with atrous separable convolution for semantic image segmentation. In *ECCV*, 2018.
- [37] Gennadii G Matvienko and Alexander Ya Sukhanov. Application of neural networks for retrieval of the co2 concentration at aerospace sensing by ipda-dial lidar. *Remote Sensing*, 11(6):659, 2019.

- [38] Hiroyuki Matsubara. An activity recognition system at home based on illuminance sensors. *Electronics and Communications in Japan*, 2023.
- [39] Bailian Chen, Dylan R Harp, Youzuo Lin, Elizabeth H Keating, and Rajesh J Pawar. Geologic co2 sequestration monitoring design: A machine learning and uncertainty quantification based approach. *Applied Energy*, 225:332–345, 2018.
- [40] Johannes Rangel, Robert Schmoll, and Andreas Kroll. On scene flow computation of gas structures with optical gas imaging cameras. In *Proceedings of the IEEE/CVF Winter Conference on Applications of Computer Vision*, pages 174–182, 2020.
- [41] Xiaodan Zhang, Xinbo Gao, Lihuo He, and Wen Lu. Mscan: Multimodal self-and-collaborative attention network for image aesthetic prediction tasks. *Neurocomputing*, 430:14–23, 2021.
- [42] Tete Xiao, Yingcheng Liu, Bolei Zhou, Yuning Jiang, and Jian Sun. Unified perceptual parsing for scene understanding. In *Proceedings of the European conference on computer vision (ECCV)*, pages 418–434, 2018.
- [43] Jonathan Long, Evan Shelhamer, and Trevor Darrell. Fully convolutional networks for semantic segmentation. In *Proceedings of the IEEE conference on computer vision and pattern recognition*, pages 3431–3440, 2015.
- [44] Yan Wang, Yusen Li, Gang Wang, and Xiaoguang Liu. Multi-scale attention network for single image super-resolution. In *Proceedings of the IEEE/CVF Conference on Computer Vision and Pattern Recognition*, pages 5950–5960, 2024.
- [45] Jie-Neng Chen, Shuyang Sun, Ju He, Philip HS Torr, Alan Yuille, and Song Bai. Transmix: Attend to mix for vision transformers. In *Proceedings of the IEEE/CVF conference on computer vision and pattern recognition*, pages 12135–12144, 2022.
- [46] Zhenyi Lu, Chenghao Fan, Wei Wei, Xiaoye Qu, Dangyang Chen, and Yu Cheng. Twin-merging: Dynamic integration of modular expertise in model merging. *Advances in Neural Information Processing Systems*, 37:78905–78935, 2024.
- [47] Zheng Ge, Zhi-Yuan Zhou, Jing-Xin Cheng, Li Chen, Yin-Hai Li, Yan Li, Su-Jian Niu, and Bao-Sen Shi. Thermal camera based on frequency upconversion and its noise-equivalent temperature difference characterization. *Advanced Photonics Nexus*, 2(4):046002–046002, 2023.
- [48] Mohamed G Embaby, Toqi Tahamid Sarker, Amer AbuGhazaleh, and Khaled R Ahmed. Optical gas imaging and deep learning for quantifying enteric methane emissions from rumen fermentation in vitro. *IET Image Processing*, 19(1):e13327, 2025.
- [49] Ze Liu, Yutong Lin, Yue Cao, Han Hu, Yixuan Wei, Zheng Zhang, Stephen Lin, and Baining Guo. Swin transformer: Hierarchical vision transformer using shifted windows. *arXiv preprint arXiv:2103.14030*, 2021.
- [50] Zhuang Liu, Hanzi Mao, Chao-Yuan Wu, Christoph Feichtenhofer, Trevor Darrell, and Saining Xie. A convnet for the 2020s. *Proceedings of the IEEE/CVF Conference on Computer Vision and Pattern Recognition (CVPR)*, 2022.
- [51] Changqian Yu, Changxin Gao, Jingbo Wang, Gang Yu, Chunhua Shen, and Nong Sang. Bisenet v2: Bilateral network with guided aggregation for real-time semantic segmentation. *International Journal of Computer Vision*, pages 1–18, 2021.
- [52] Huihui Pan, Yuanduo Hong, Weichao Sun, and Yisong Jia. Deep dual-resolution networks for real-time and accurate semantic segmentation of traffic scenes. *IEEE Transactions on Intelligent Transportation Systems*, 2022.
- [53] Rudra PK Poudel, Stephan Liwicki, and Roberto Cipolla. Fast-scnn: Fast semantic segmentation network. *arXiv preprint arXiv:1902.04502*, 2019.
- [54] Meng-Hao Guo, Cheng-Ze Lu, Qibin Hou, Zhengning Liu, Ming-Ming Cheng, and Shi-Min Hu. Segnext: Rethinking convolutional attention design for semantic segmentation. *arXiv preprint arXiv:2209.08575*, 2022.
- [55] Min Bai and Raquel Urtasun. Deep watershed transform for instance segmentation. In *Proceedings of the IEEE conference on computer vision and pattern recognition*, pages 5221–5229, 2017.
- [56] MMSegmentation Contributors. MMSegmentation: Openmmlab semantic segmentation toolbox and benchmark. <https://github.com/open-mmlab/mms Segmentation>, 2020.

## A Appendix

### A.1 CCR Dataset

CCR dataset consists of thermal images capturing CO<sub>2</sub> gas releases under controlled laboratory conditions across various flow rates (10-100 SCCM). As shown in Figure 6, the dataset includes thermal images and their corresponding ground truth masks at different flow rates, demonstrating the varying visual characteristics of CO<sub>2</sub> plumes. The images were captured using a FLIR G343 thermal camera primarily in White hot mode, where CO<sub>2</sub> appears as bright regions against a darker background due to its thermal absorption properties.

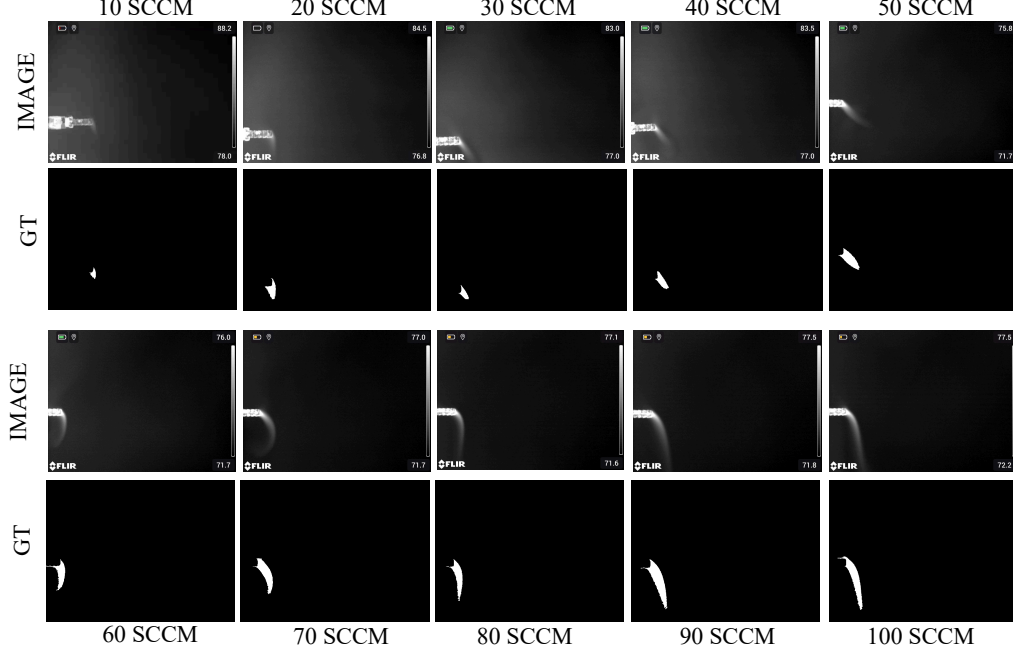


Figure 6: Sample images from the CCR dataset showing CO<sub>2</sub> releases at different flow rates (10-100 SCCM). For each flow rate, the top row shows the thermal image (IMAGE) and its corresponding ground truth mask (GT). The dataset captures the progressive changes in plume morphology and intensity as flow rates increase, demonstrating the challenging nature of CO<sub>2</sub> detection across varying conditions.

Table 4: Distribution of CCR dataset across different CO<sub>2</sub> flow rates (SCCM). The dataset includes multiple thermal visualization modes from FLIR G343 camera, with White hot being the primary mode for CO<sub>2</sub> plume visualization.

Flow Rate	Train	Test	Val	Color Modes
10	1,048	131	133	White hot
20	1,100	137	139	White hot, Black hot
30	1,380	173	173	White hot
40	1,427	177	180	White hot
50	1,561	194	197	White hot
60	1,928	241	241	White hot, Lava
70	1,808	225	228	White hot
80	1,636	204	206	White hot, Lava
90	1,770	221	223	White hot
100	2,119	264	267	White hot, Black hot
Total	14,777	1,967	1,987	–

Table 5: Per class IoU results on CCR dataset. Class labels represent CO<sub>2</sub> flow rates in SCCM.

Model	BG	10	20	30	40	50	60	70	80	90	100
BiseNetV2 [51]	99.86	69.09	69.92	76.36	57.88	62.68	78.87	73.29	69.49	85.03	81.90
DDRNet [52]	99.83	63.77	67.47	74.32	59.55	62.84	75.16	70.54	70.74	84.02	79.54
FastSCNN [53]	99.84	16.02	0.14	0.00	49.15	31.75	74.39	65.82	55.60	81.96	76.99
SegFormer-B0 [32]	99.88	70.03	78.48	82.56	78.31	79.36	86.35	85.97	82.51	88.69	84.84
SegNeXt [54]	99.89	69.70	80.59	81.76	69.62	72.04	85.10	85.48	86.79	89.81	87.29
<b>CarboFormer (Ours)</b>	99.88	71.25	80.21	82.90	81.77	82.12	86.94	84.10	83.75	89.35	86.33
DeepLabv3+ [36]	99.85	68.49	77.04	80.24	76.32	77.34	82.61	84.63	81.08	84.78	80.18
Swin-T [49]	99.89	69.37	79.90	83.22	78.03	80.44	86.22	86.17	84.67	89.66	86.06
ConvNeXt-S [50]	99.90	84.10	82.54	85.11	88.07	84.38	86.14	86.47	82.74	86.01	86.80
SegFormer-B5 [32]	99.90	70.50	77.80	84.01	86.76	89.22	87.59	89.67	89.18	90.32	87.98
<b>CarboNeXT (Ours)</b>	<b>99.93</b>	<b>80.85</b>	<b>82.08</b>	<b>87.86</b>	<b>85.20</b>	<b>84.02</b>	<b>83.71</b>	<b>90.43</b>	<b>91.26</b>	<b>92.49</b>	<b>89.48</b>

Table 6: Per class Fscore results on CCR dataset. Class labels represent CO<sub>2</sub> flow rates in SCCM.

Model	BG	10	20	30	40	50	60	70	80	90	100
BiseNetV2 [51]	99.93	81.72	82.30	86.60	73.32	77.06	88.19	84.58	82.00	91.91	90.05
DDRNet [52]	99.91	77.88	80.58	85.27	74.65	77.18	85.82	82.73	82.86	91.32	88.60
FastSCNN [53]	99.92	27.61	0.28	–	65.91	48.20	85.32	79.39	71.47	90.09	87.00
SegFormer-B0 [32]	99.94	82.37	87.94	90.45	87.83	88.49	92.68	92.46	90.42	94.01	91.80
SegNeXt [54]	99.94	82.14	89.25	89.96	82.09	83.74	91.95	92.17	92.93	94.63	93.21
<b>CarboFormer (Ours)</b>	99.94	83.12	88.83	90.63	89.99	89.92	93.41	91.17	91.10	94.56	92.75
DeepLabv3+ [36]	99.92	81.30	87.03	89.04	86.57	87.22	90.48	91.67	89.55	91.76	89.00
Swin-T [49]	99.94	81.92	88.83	90.84	87.66	89.16	92.60	92.57	91.70	94.55	92.50
ConvNeXt-S [50]	99.95	91.36	90.44	91.96	93.66	91.53	92.55	92.75	90.55	92.48	92.93
SegFormer-B5 [32]	99.95	82.70	87.51	91.31	92.91	94.30	93.38	94.56	94.28	94.91	93.60
<b>CarboNeXT (Ours)</b>	<b>99.96</b>	<b>89.41</b>	<b>90.16</b>	<b>93.54</b>	<b>92.01</b>	<b>91.32</b>	<b>91.13</b>	<b>94.98</b>	<b>95.43</b>	<b>96.10</b>	<b>94.45</b>

Table 4 presents the detailed distribution of the CCR dataset, comprising 15,777 images split across training (14,777), testing (1,967), and validation (1,987) sets. The dataset is carefully balanced across different flow rates, with a slight emphasis on higher flow rates (60-100 SCCM) to capture more complex plume behaviors. While White hot is the primary thermal visualization mode, some flow rates include additional color modes (Black hot, Lava) to enhance dataset diversity and model robustness. This multi-modal approach particularly benefits the training of models for real-world deployment where varying thermal visualization settings may be encountered.

## B More Performance Evaluation

### B.1 Training Strategy

Both CarboNeXT and CarboFormer share common preprocessing configurations, using SyncBN and LayerNorm for normalization, with input images normalized using mean [123.675, 116.28, 103.53] and standard deviation [58.395, 57.12, 57.375]. During training, images are processed at 512×512 pixels with a size divisor of 32 for testing. Both models employ a dropout strategy with drop path rate of 0.1, though CarboNeXT uses a base rate of 0.0. The key differences lie in their decoder configurations and optimization approaches. CarboNeXT’s UPerHead decoder operates with 512 channels and pool scales of (1, 2, 3, 6), while CarboFormer uses a lightweight design with optimized attention kernel paddings. For optimization, CarboFormer employs the AdamW optimizer with a learning rate of  $6 \times 10^{-5}$ , betas of (0.9, 0.999), and weight decay of 0.01, combined with a specialized learning rate schedule incorporating linear warm-up and polynomial decay. Both models use CrossEntropyLoss in their decoder and auxiliary heads, with weights 1.0 and 0.4 respectively.

### B.2 Classwise Performance Analysis on CCR Dataset

We conduct a comprehensive analysis of model performance across different CO<sub>2</sub> flow rates, with particular attention to challenging low-flow scenarios (10-50 SCCM). As shown in Tables 5 and 6, CarboNeXT demonstrates remarkable improvements over existing methods, particularly in the challenging task of detecting subtle thermal signatures at low flow rates. The performance gap between CarboNeXT and previous state-of-the-art models like SegFormer-B5 [32] is most pronounced in these low-flow conditions, where accurate detection is crucial for early emission identification. Similarly, CarboFormer proves to be an effective lightweight alternative, maintaining consistent performance across the low-flow range while requiring significantly fewer computational resources.

At higher flow rates (60-100 SCCM), both models continue to excel, with CarboNeXT achieving its peak performance at 90 SCCM and CarboFormer showing competitive results. As visualized in Figure 5, our models demonstrate exceptional stability in plume detection and boundary delineation across varying flow conditions. This consistent performance stands in stark contrast to baseline models like FastSCNN [53], which catastrophically fails at flow rates 20-30 SCCM (IoU: 0.14% and 0.00% respectively), indicating complete confusion in distinguishing CO<sub>2</sub> plumes at these critical flow rates. The robust background discrimination capabilities of both models further enhance their practical utility by minimizing false positives, making them reliable solutions for real-world CO<sub>2</sub> monitoring applications.

Table 7: Per class results on RTA dataset showing background and gas segmentation performance.

Model	IoU		Fscore	
	Background	Gas	Background	Gas
BiseNetV2 [51]	94.43	81.48	97.13	89.79
DDRNet [52]	94.57	81.98	97.21	90.10
FastSCNN [53]	94.22	80.14	97.02	88.98
SegFormer-B0 [32]	96.43	88.26	98.18	93.77
SegNeXt [54]	95.84	86.47	97.87	92.75
<b>CarboFormer (Ours)</b>	<b>97.75</b>	<b>89.35</b>	<b>98.00</b>	<b>94.11</b>
DeepLabv3+ [36]	96.17	87.18	98.05	93.15
Swin-T [49]	95.84	86.47	97.87	92.74
ConvNeXt-S [50]	94.75	85.60	96.40	90.95
SegFormer-B5 [32]	96.66	89.02	98.30	94.19
<b>CarboNeXT (Ours)</b>	<b>96.51</b>	<b>89.41</b>	<b>98.85</b>	<b>94.26</b>

### B.3 Classwise Performance Analysis on RTA Dataset

The RTA dataset presents a binary segmentation task focusing on distinguishing CO<sub>2</sub> gas plumes from the background. As detailed in Table 7, both our proposed models demonstrate exceptional capabilities in this challenging binary classification scenario. CarboNeXT sets a new state-of-the-art benchmark, marginally outperforming sophisticated architectures like SegFormer-B5 [32], while showing substantial improvements over lightweight alternatives such as FastSCNN [53]. CarboFormer proves particularly impressive, achieving comparable performance to heavyweight models while maintaining its computational efficiency advantage.

A standout feature of both models is their robust background discrimination capabilities, which is crucial for practical CO<sub>2</sub> leak detection applications. The high F-scores achieved by both models underscore their reliability in distinguishing gas plumes from background thermal patterns, making them particularly valuable for real-world deployment scenarios where false positives must be minimized.

### B.4 Performance Stability and Reliability Analysis

To validate the stability and reliability of our results, we conducted 5 independent training runs with different random seeds while maintaining consistent hyperparameters (learning rate:  $6 \times 10^{-5}$ , batch size: 2) and training conditions (160,000 iterations). The reported standard deviations capture variations from both initialization and optimization trajectories.

Table 8: Performance stability analysis showing mean and standard deviation across 5 runs with 95% confidence intervals ( $2\sigma$ ). Results demonstrate overall model reliability across different metrics.

Model	mIoU (%)	mAcc (%)	mFscore (%)
CarboNeXT	88.46 $\pm$ 0.31	91.04 $\pm$ 0.28	93.81 $\pm$ 0.25
CarboFormer	84.88 $\pm$ 0.42	91.13 $\pm$ 0.35	91.90 $\pm$ 0.38

Table 9: Classwise stability analysis showing IoU  $\pm$  standard deviation across 5 runs for different CO<sub>2</sub> flow rates (SCCM).

Model	BG	10	20	30	40	50	60	70	80	90	100
CarboNeXT	99.93 $\pm 0.02$	80.85 $\pm 0.42$	82.08 $\pm 0.38$	87.86 $\pm 0.35$	85.20 $\pm 0.39$	84.02 $\pm 0.38$	83.71 $\pm 0.36$	90.43 $\pm 0.32$	91.26 $\pm 0.30$	92.49 $\pm 0.29$	89.48 $\pm 0.31$
CarboFormer	99.88 $\pm 0.03$	71.25 $\pm 0.51$	80.21 $\pm 0.48$	82.90 $\pm 0.45$	81.77 $\pm 0.47$	82.12 $\pm 0.45$	86.94 $\pm 0.42$	84.10 $\pm 0.43$	83.75 $\pm 0.41$	89.35 $\pm 0.37$	86.33 $\pm 0.39$

Our stability analysis reveals that both models demonstrate robust reliability across multiple runs, with CarboNeXT showing exceptional consistency in its predictions. The classwise analysis in Table 9 highlights this stability across different flow rates, with both models achieving remarkable precision in background detection (standard deviations of  $\pm 0.02\%$  for CarboNeXT and  $\pm 0.03\%$  for CarboFormer). For CO<sub>2</sub> detection, while variability naturally increases at challenging low flow rates (10-30 SCCM) due to subtle thermal signatures, CarboNeXT maintains notably lower variability ( $\pm 0.42\%$  at 10 SCCM) compared to CarboFormer ( $\pm 0.51\%$ ). Both models demonstrate increased stability at higher flow rates (80-100 SCCM), and paired t-tests confirm the statistical significance of their performance improvements ( $p < 0.01$ ), validating the robustness of our architectural designs for practical CO<sub>2</sub> monitoring applications.

## C Broader Impacts

This research advances CO<sub>2</sub> leak detection capabilities with significant implications for environmental monitoring and industrial safety. Our models’ ability to detect CO<sub>2</sub> at low flow rates (as low as 10 SCCM) could substantially improve early warning systems for carbon capture and storage facilities, while CarboFormer’s lightweight nature enables real-time monitoring through mobile platforms like drones for inspecting remote infrastructure. Beyond industrial applications, this technology could enhance climate science research by enabling more accurate tracking of natural CO<sub>2</sub> emissions from geological sources. While our models enhance detection capabilities, they should be integrated within comprehensive safety systems rather than used as standalone solutions. Despite potential privacy considerations in populated areas, we believe the environmental and safety benefits of improved CO<sub>2</sub> detection are crucial for addressing modern climate change challenges.

## D Limitations

While our proposed models demonstrate promising results, several key limitations should be acknowledged. First, our models were primarily evaluated under controlled laboratory conditions, and their performance in diverse environmental settings (varying humidity, wind conditions, or ambient temperatures) remains to be thoroughly validated. Second, the limited size of the RTA dataset (613 images) may restrict the models’ generalization capabilities in real-world industrial settings, despite our transfer learning approach. Additionally, while CarboFormer achieves competitive performance as a lightweight model, there is potential room for improvement in its accuracy, particularly at low flow rates, possibly through more sophisticated knowledge distillation techniques or architectural optimizations.

## E Future Work

Our ongoing and future research directions focus on several key expansions of the current work. We are actively working to extend the RTA dataset by incorporating samples with varying pH values, which will help understand the models’ performance across different chemical conditions. A significant upcoming effort involves data collection from real farm environments, specifically targeting CO<sub>2</sub> emissions from the dairy cow, which will provide valuable real-world validation of our detection systems. Additionally, we plan to broaden the scope of our gas detection capabilities to include other environmentally significant gases such as methane and butene across different flow rates.